Orientational correlations and the effect of spatial gradients in the equilibrium steady state of hard rods in two dimensions: A study using deposition-evaporation kinetics

Mahendra D. Khandkar and Mustansir Barma
Department of Theoretical Physics, Tata Institute of Fundamental Research, Homi Bhabha Road, Colaba, Mumbai-400 005, India
(Received 25 January 2005; revised manuscript received 18 May 2005; published 28 November 2005)

Deposition and evaporation of infinitely thin hard rods (needles) is studied in two dimensions using Monte Carlo simulations. The ratio of deposition to evaporation rates controls the equilibrium density of rods, and increasing it leads to an entropy-driven transition to a nematic phase in which both static and dynamical orientational correlation functions decay as power laws, with exponents varying continuously with deposition-evaporation rate ratio. Our results for the onset of the power-law phase agree with those for a conserved number of rods. At a coarse-grained level, the dynamics of the nonconserved angle field is described by the Edwards-Wilkinson equation. Predicted relations between the exponents of the quadrupolar and octupolar correlation functions are borne out by our numerical results. We explore the effects of spatial inhomogeneity in the deposition-evaporation ratio by simulations, entropy-based arguments, and a study of the additional terms introduced in the free energy. The primary effect is that needles tend to align along the local spatial gradient of the ratio. A uniform gradient thus induces a uniformly aligned state, as does a gradient which varies randomly in magnitude and sign, but acts only in one direction. Random variations of deposition-evaporation rates in both directions induce frustration, resulting in a state with glassy characteristics.
DOI: 10.1103/PhysRevE.72.051717 PACS number(s): 64.70.Md, 64.60.Cn

I. INTRODUCTION

An assembly of particles interacting via hard-core repulsion serves as a useful model for studying simple fluids, colloids, liquid crystals, and many other soft matter systems. The analysis of such model systems helps in understanding the features of real systems, such as their phase behavior and structural and dynamic properties. An important role is played by the anisotropy of shape of the constituent particles, which can range from thick elongated platelets to thin rods. Some examples of systems in which the constituent particles show anisotropy are certain types of colloids, liquid crystals, and protein molecules. In particular, rodlike particles are found in suspensions of the tobacco mosaic virus [1], nematic liquid crystals [2], and, recently, carbon nanotube gels [3]. All these systems show very rich and characteristic phase behavior.

Rodlike particles have been modeled theoretically as ellipses [4], rectangles, and spherocylinders [5–7] with varying aspect ratios, a limiting case being infinitely thin hard rods or needles [8]. These systems exhibit a number of interesting entropy-driven phase transitions which have been studied in two and three dimensions, usually using simulations with number-conserving dynamics. On the other hand, there are a number of physical processes that involve adsorption (deposition) and desorption (evaporation) of particles, which do not conserve particle number, and which are important for some monolayer growth processes. Adsorption and desorption are also important in the binding and unbinding of ligands with microtubules, the interaction of proteins with DNA [9,10], and many catalytic reactions. Finally, in recent experiments on assemblies of long objects (rice grains, thin metal rods) on a vibrating plate [11], individual particles jump off and return to the plate, leading ultimately to a state with interesting patterns. These considerations motivate us to study the deposition and evaporation of hard objects with rigid boundaries on a substrate. While a deposition-only system, of the type studied in random sequential adsorption [9], can end up in a nonevolving jammed configuration, with the addition of evaporation, the system eventually reaches an equilibrium steady state with a density governed by the rates of deposition and evaporation [12–17]. While most of these studies have focused on the kinetics of approach to steady state, in this paper, we are interested in the properties of the steady state itself. Specifically, we study the patterns formed due to deposition and evaporation of infinitely thin hard rods (needles) on a two-dimensional (2D) substrate. Needles are a limiting case of rodlike particles in the systems mentioned earlier. Though not directly applicable to any physical system, this is an important limiting case; the limit of zero width simplifies the problem by eliminating the aspect ratio as a parameter. The hard-core constraint is enforced by rejecting any deposition event that results in an overlap of needles.

It is useful to recall some known facts about a system of hard needles with no externally imposed spatial inhomogeneities. This system shows a transition from a low-density orientationally disordered (isotropic) state to a high-density ordered state with nematic correlations. This transition, whose existence was pointed out by Onsager [18], can be viewed as an outcome of the interplay between orientational and translational entropy of the needles; the ordered (aligned) state is preferred at high density since alignment leads to an increase of translational entropy, albeit at the cost of orientational entropy. The nature of the orientational ordering is dimension dependent. In three dimensions, orientational long range order (LRO) sets in. A state with LRO would break the continuous symmetry of rotations, and is thus not expected to occur in 2D, even though the Mermin-Wagner theorem cannot be generalized to this system [19]. Indeed, the simulation study of Frenkel and Eppenga [8] on a system with a fixed number of needles confirms the absence of LRO in 2D, and finds a phase with power-law decays of orientational correlations, quite analogous to the *XY* model [20].

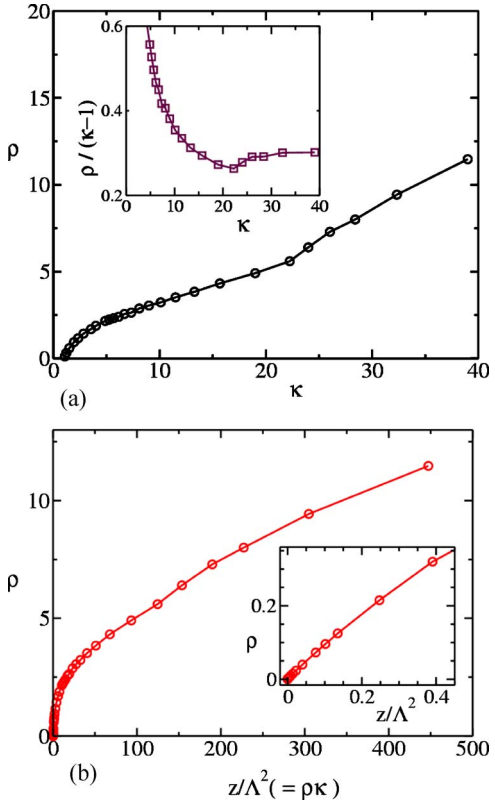

FIG. 1. (Color online) (a) The variation of ρ (number of rods per unit area) with κ shows a change of behavior for κ in the range 20–25. This is more prominently depicted in the inset which shows the variation of $\rho/(\kappa-1)$. (b) Variation of ρ with z/Λ^2. The inset shows the initial portion of the curve.

On a coarse-grained scale, the local orientation at location $\mathbf{r}$ and time t is specified by an angle field $\theta(\mathbf{r},t)$. The orientational correlation functions of interest are defined as

$$g_\ell(\mathbf{r},t) = \langle \cos\{\ell[\theta(\mathbf{r},t) - \theta(0,0)]\}\rangle \tag{1}$$

where ℓ is an even integer, and θ and $\theta+\pi$ represent the same state. Quadrupolar correlations are probed by $\ell=2$, whereas higher values of ℓ correspond to higher multipolarities. From numerical simulations, we find power-law decays in both space and time: $g_\ell(r,0)\sim r^{-\eta_\ell}$ and $g_\ell(0,t)\sim t^{-\beta_\ell}$ for both $\ell=2$ and 4. Our results for the static correlations conform to the Kosterlitz-Thouless theory for the onset of correlations, while our results for the dynamics show that their decay in time is governed by the Edwards-Wilkinson equation. We also study spatial variations of the deposition rate, and find strong effects on the nature of the ordering. We consider several types of variations: (i) a sharp change across a linear interface; (ii) a smooth linear gradient; (iii) a random variation of rates in one direction; and (iv) random variation of rates in the plane. We find that the qualitative effect of spatial variations is to induce alignment of needles in the direction of the gradient, an effect with an entropic origin. In (i), the effect dies down slowly with increasing distance from the interface, but in cases (ii) and (iii) it results in a state with overall alignment along the direction of variation of the deposition rate. The random variation in (iv) induces frustration and the result is then a state with glassy features such as strong initial condition dependence and slow relaxation.

II. MODEL AND PROCEDURE

In our model, infinitely thin hard rods (needles) are added to a 2D substrate with area A with a constant attempt rate, and simultaneously removed randomly from the substrate with a specified rate. In a deposition attempt, the location of the centre of mass of the needle is chosen at random on the substrate, and the orientation angle is chosen at random as well. Let Γ_d be the rate of attempted depositions per unit area per unit angle interval. An attempt is successful only if the depositing needle in question would not overlap with existing needles on the substrate; otherwise it is rejected.

During evaporation, a needle is chosen at random from those present on the substrate and then removed. If the total rate of such removals is R_e we may associate a removal rate $\Gamma_e = R_e/2\pi A$ per unit area per unit angle interval. The ratio

$$\kappa = \frac{\Gamma_d}{\Gamma_e} \tag{2}$$

of deposition to evaporation rates is the control parameter in the problem. As we show below, κ is related to the fugacity $z=e^{\beta\mu}$ of an equilibrium grand canonical system.

The model under consideration can be thought of as describing the adsorption and release of needlelike gas molecules on a substrate in contact with a gas reservoir with which it can exchange particles. The equilibrium state on the substrate is then described by the grand canonical (μAT) ensemble, where μ, A, and T are, respectively, the chemical potential, substrate area, and temperature. Define scaled coordinates $\mathbf{s}_i = \mathbf{r}_i/L$, where $\mathbf{r}_i$ is the position of the ith particle on the substrate and L is the linear dimension of the system. The grand canonical partition function can be written [21] as

$$\mathcal{Z} = \sum_{N=0}^{\infty} \frac{z^N}{N!}(A/\Lambda^2)^N \int d\mathbf{s}_1 \int d\mathbf{s}_2 \cdots \int d\mathbf{s}_N \times \int d\theta_1 \int d\theta_2 \cdots \int d\theta_N e^{-\beta U(\mathbf{s}_1,\mathbf{s}_2,\ldots,\mathbf{s}_N,\theta_1,\theta_2,\ldots,\theta_N)} \tag{3}$$

where $\Lambda = (2\pi\hbar^2/mk_BT)^{1/2}$ is the thermal wavelength which results from integrating over the momentum of needles, and U is the interaction energy for a configuration in which there are N needles with scaled center of mass locations $(\mathbf{s}_1,\mathbf{s}_2,\ldots,\mathbf{s}_N)$ and orientations $(\theta_1,\theta_2,\ldots,\theta_N)$. The corresponding equilibrium probability density of a configuration $C \equiv (\mathbf{s}_1,\mathbf{s}_2,\ldots,\mathbf{s}_N,\theta_1,\theta_2,\ldots,\theta_N)$ is [21]

$$P_{eq}(C) = \frac{1}{\mathcal{Z}}\frac{z^N}{N!}(A/\Lambda^2)^N e^{-\beta U(\mathbf{s}_1,\mathbf{s}_2,\ldots,\mathbf{s}_N,\theta_1,\theta_2,\ldots,\theta_N)}. \tag{4}$$

For our system of hard-core needles, the interaction energy $U\to\infty$ when needles overlap, while $U=0$ when there is no overlap between any needles. Thus all allowed configurations with fixed N have equal weights.

Deposition-evaporation dynamics involves changes of N. The evolution from a configuration C to a configuration C' can be described by the master equation

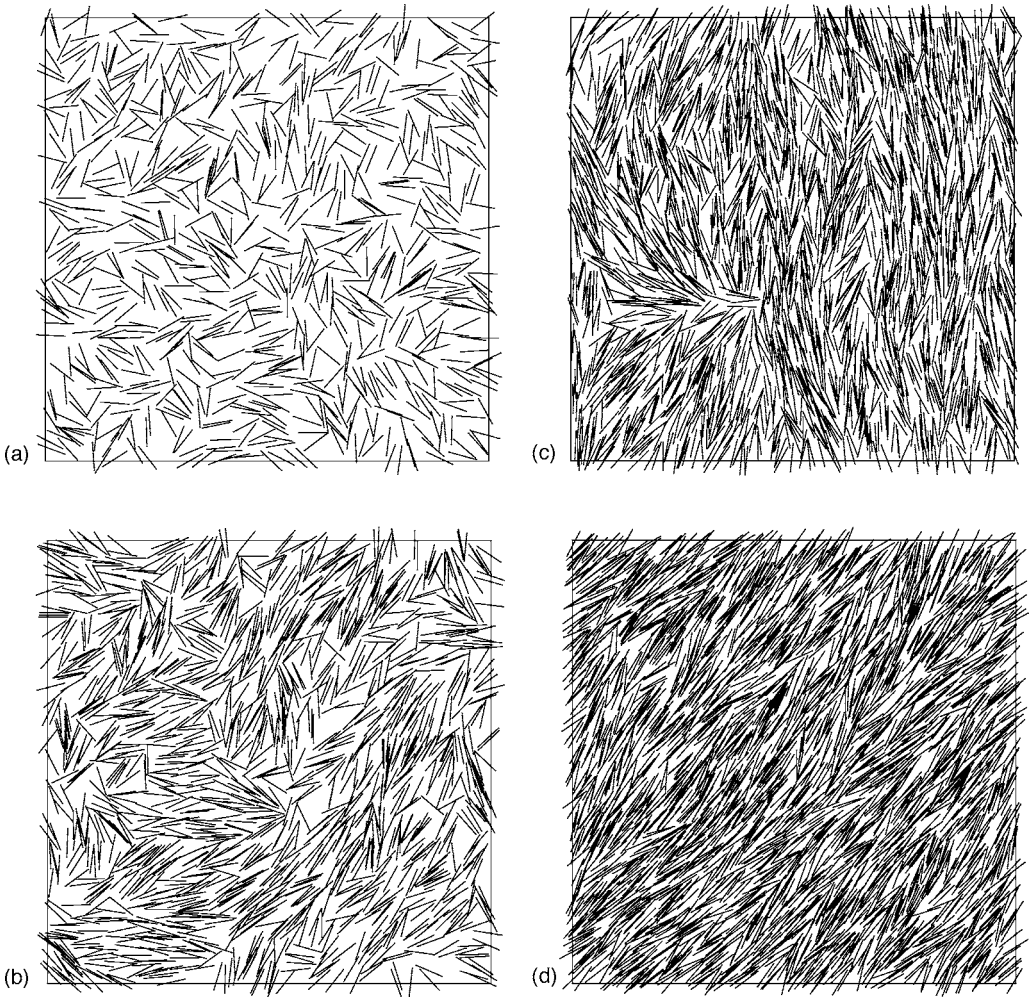

FIG. 2. Snapshots of hard-rod configurations at different values of κ, (a) 19, (b) 24, (c) 32, and (d) 39. The substrate size is 15×15. Observe the formation of defects in the configurations (a), (b), and (c).

$$\frac{\partial P(C)}{\partial t} = \sum_{C'} [P(C')W(C' \to C) - P(C)W(C \to C')]. \quad (5)$$

The steady state of Eq. (5), obtained by setting $\partial P(C)/\partial t = 0$, is in fact an equilibrium state if the condition of detailed balance

$$\frac{W(C' \to C)}{W(C \to C')} = \frac{P_{eq}(C)}{P_{eq}(C')} \quad (6)$$

is satisfied for every pair of configurations C and C' that can be reached from each other. Now, let C denote an N-needle configuration and let C' be the $(N-1)$-needle configuration obtained from C by removing a particular needle. Using Eq. (4) in Eq. (6), we see that $\Gamma_d/\Gamma_e = zA/\Lambda^2 N$. Thus, the steady state of deposition-evaporation dynamics is described by the grand canonical equilibrium state with

$$\kappa = \frac{z}{\rho\Lambda^2} \quad (7)$$

where $\rho = N/A$ is the areal density of needles.

In our Monte Carlo studies we varied the control parameter κ in the range 1 to 40 and monitored the resulting density and orientational correlations. We used an $L\times L$ substrate (with $L=15$ and 25) where L is in units of needle length. For each value of κ we made multiple runs, allowing up to 10^7 Monte Carlo time steps for equilibration. The Monte Carlo time t is defined as the number of attempts

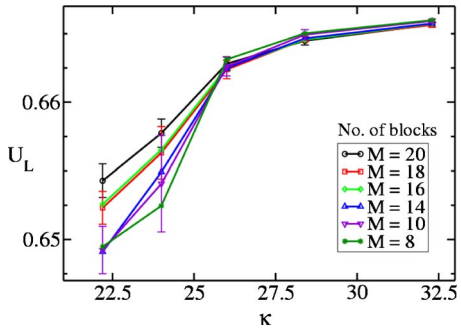

FIG. 3. (Color online) Orientational cumulants U_L as a function of deposition-evaporation ratio κ for various subsystem sizes $L=K/M$. Note the collapse of the curves beyond $\kappa_c \simeq 25$, pointing to the occurrence of a power-law phase.

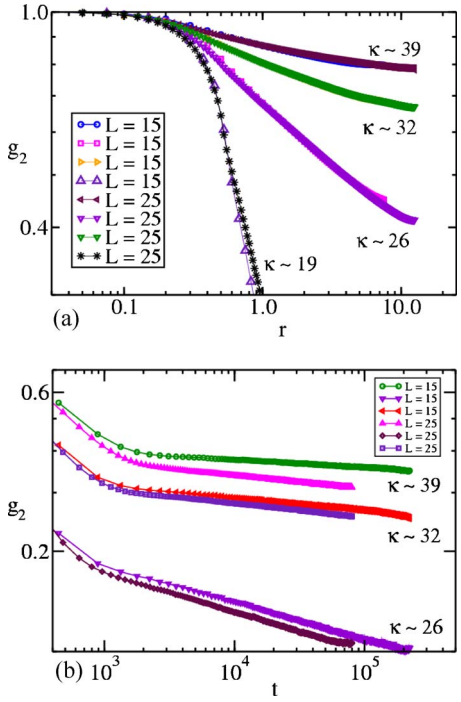

FIG. 4. (Color online) Log-log plots of (a) $g_2(r,0)=\langle\cos\{2[\theta(r,t)-\theta(0,t)]\}\rangle$ and (b) $g_2(0,t)=\langle\cos\{2[\theta(r,t)-\theta(r,0)]\}\rangle$ showing the static and temporal behavior, respectively, of $g_2(r,t)$. Data are shown for systems of sizes 15×15 and 25×25, and different values of κ. The distance r is in units of rod length and time t is in Monte Carlo time steps.

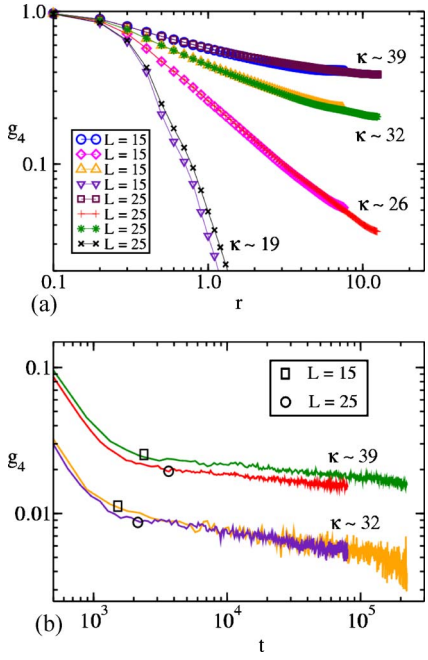

FIG. 5. (Color online) Log-log plots of (a) $g_4(r,0)=\langle\cos\{4[\theta(r,t)-\theta(0,t)]\}\rangle$ and (b) $g_4(0,t)=\langle\cos\{4[\theta(r,t)-\theta(r,0)]\}\rangle$ showing the static and temporal behavior, respectively, of $g_4(r,t)$, for the same system sizes and values of κ as in Fig. 4.

divided by L^2. Averaging was done over 10 sets of independent runs and 1000 configurations from each run after equilibration.

Figure 1(a) shows the variations of the density with κ, while Fig. 1(b) shows ρ plotted against $z/\Lambda^2=\rho\kappa$. The inset in Fig. 1(a) shows a marked change in the dependence of $\rho/(\kappa-1)$ on κ for κ in the range 20–25. As we shall see, there is a transition to a phase with power-law decay of orientational correlations beyond $\kappa=\kappa_c\simeq25$, as illustrated by the representative configurations shown in Fig. 2 for different values of κ. We turn to a quantitative study of orientational ordering in the next section.

III. ORIENTATIONAL ORDERING

A. Order parameter

For a system of N hard rods in 2D, the nematic order parameter q is given by

$$q=\frac{1}{N}\left\langle\sum_{i=1}^{N}\cos(2\theta_i)\right\rangle \tag{8}$$

where θ_i is the angle made by the ith rod with the nematic director, which itself has an orientation ϕ with respect to a fixed reference X axis. Both ϕ and q can be found by studying the tensor order parameter defined as

$$\mathbf{Q}_{\alpha\beta}=\frac{1}{N}\left\langle\sum_{i=1}^{N}[2u_\alpha(i)u_\beta(i)-\delta_{\alpha\beta}]\right\rangle \tag{9}$$

where $u_\alpha(i)$ is the αth component of $\mathbf{u}(i)$, the vector specifying the orientation of the ith rod. The eigenvalues of $\mathbf{Q}_{\alpha\beta}$ are $\pm q$, and the corresponding eigenvectors pick out directions along and perpendicular to the director orientation ϕ. Insofar as there is no long-range order in the 2D needle system, q vanishes in the thermodynamic limit. In simulations on finite systems, though, q may appear to be nonzero [Fig. 2(d)], over short times. Tracking the onset of such an apparent value is not a reliable way to locate the transition point.

TABLE I. κ dependence of exponents η_ℓ and β_ℓ for $\ell=2$ and 4. The estimated error is indicated in parentheses.

κ	ρ	η_2	η_4	β_2	β_4	K/B
26.0	7.3	0.23 (0.03)	0.87 (0.06)	0.11 (0.04)	0.31 (0.06)	5.3×10^{-3}
32.3	9.4	0.098 (0.006)	0.41 (0.02)	0.037 (0.007)	0.16 (0.04)	12.8×10^{-3}
39.0	11.4	0.059 (0.003)	0.25 (0.01)	0.022 (0.003)	0.09 (0.01)	21.4×10^{-3}

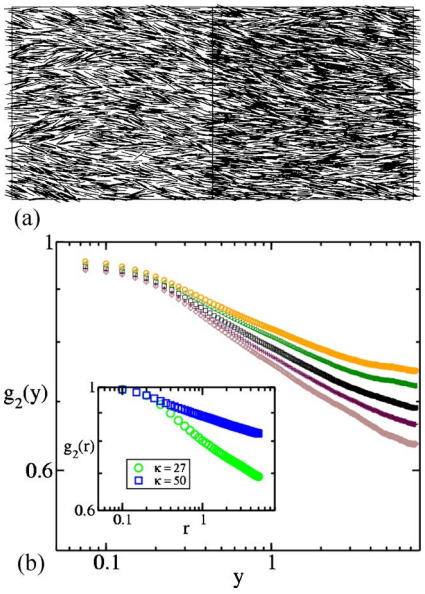

FIG. 6. (Color online) (a) Snapshot of a typical hard-rod configuration with a single κ_1-κ_2 interface. The system size is 25×15 and $\kappa_1=30$ (left half) and $\kappa_2=50$ (right half). Boundary conditions: open (along X); periodic (along Y). Notice the difference in density in the two halves. (b) This plot shows the decay of the orientational correlation function $g_2(\mathbf{y})=\langle\cos\{2[\theta(\mathbf{y})-\theta(0)]\}\rangle$ calculated for a pair of points in the same vertical strip of unit width. Curves from bottom to top correspond to different strips in two halves in the configuration (a). The inset shows $g_2(\mathbf{r})=\langle\cos\{2[\theta(\mathbf{r})-\theta(0)]\}\rangle$ measured radially for a box of size 6×6 which is positioned at the center of each of the left and right halves of the same configuration. The distances r and y are in units of rod length.

B. Orientational cumulant of q

A better indication of the transition point, and also the nature of the ordered phase, is provided by monitoring the probability distribution functions $P_L(q)$ of q, where q is the block-averaged value of the local order parameter with the system divided into blocks of finite size L [22]. A measure of the non-Gaussian character of $P_L(q)$ is provided by the reduced fourth order Binder cumulant of q

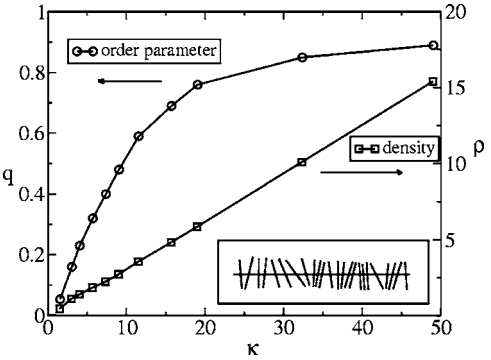

FIG. 8. Variation of the density (ρ) and order parameter (q) with κ for the 1D model which is a limiting case of the 2D κ_1-κ_2 model for Fig. 7. As shown schematically in the inset, the preferred orientation of needles is perpendicular to the line.

$$U_L = 1 - \frac{\langle q^4\rangle_L}{3\langle q^2\rangle_L^2} \tag{10}$$

where L is the linear size of the subsystem (block). U_L provides a useful diagnostic tool to monitor the ordering induced by varying κ [23].

For $L\ll\xi$, U_L is expected to stay close to a fixed point value U^*. Thus, the occurrence of a critical point with $\xi=\infty$ can be identified by plotting U_L against κ for various values of L, and looking for common intersection point.

We analyzed the Monte Carlo data of our model by monitoring U_L [Eq. (10)]. The analysis was performed as follows. We simulated a single large system of size $K\times K$ ($K=25$) and divided it into subsystems of size $L\times L$, thereby having total M^2 number of subsystems with $M=K/L$ [24]. Then, M was incremented in integer steps starting from 1 and U_L was estimated for those subsystem sizes L where a good analysis is possible. Consequently, we did not consider very small or very large values of M. Also, the curve for $M=12$ lies anomalously low and was not included. The number of subsystems (M) we use for estimating the cumulant range from 8 to 20. Figure 3 shows the variation of U_L as a function of κ for various values of L.

Below $\kappa_c\simeq25.8$, the curves are separate and distinct, but they collapse at κ_c, indicating the onset of ordering (Fig. 3). Moreover, the curves seem to stay collapsed for $\kappa>\kappa_c$ suggesting that ξ remains infinite in this phase, i.e., this is a

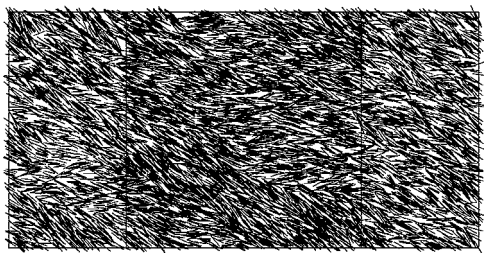

FIG. 7. A dual-interface configuration in an (80×15)-sized system with periodic boundary conditions in both directions. The middle half of size 40×15 and with $\kappa_2=50$ separates two quarters, linked at the boundary, each of size 20×15 and having $\kappa_1=30$.

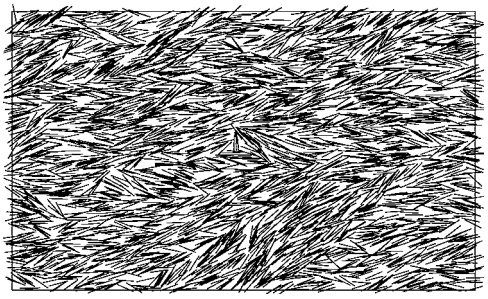

FIG. 9. A typical configuration of size 25×15 with uniform $\kappa=27$ and open boundary conditions along the X direction. Free boundaries induce alignment which propagates some distance into the bulk.

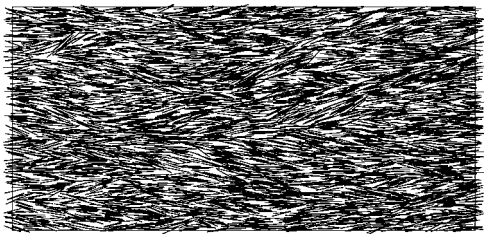

FIG. 10. A typical configuration for a (25×15)-sized system with a uniform κ gradient, with $\kappa_L=32$ and $\kappa_R=50$ at the two ends respectively. The horizontal alignment induced by the gradient is evident.

phase with power-law decay of correlations. Corroboration of this is provided by directly monitoring the correlation functions as described below.

C. Orientational correlation functions

Let us define a general orientational correlation function $g_\ell(\mathbf{r},t)=\langle\cos\{\ell[\theta(\mathbf{r},t)-\theta(0,0)]\}\rangle$ where ℓ is an even integer. We studied static and dynamical properties by investigating $g_\ell(r,0)$ and $g_\ell(0,t)$. We calculated spatial correlations by forming circular bins around each rod in turn, computing $g_\ell(r,0)$ for each bin, repeating this process for all rods in the configuration and averaging over all rods (see Fig. 4). The dynamical correlation function, $g_\ell(0,t)$ was calculated by coarse graining. The system was divided into a number of small cells (1×1) and an average value of orientation was assigned to each cell by averaging over the orientations of those needles whose centers of mass lie in the cell. The value of $g_\ell(0,t)$ was computed using this average value over each time frame, and averaging over all the cells (see Fig. 5). The initial drops of the curves in Figs. 4(b) and 5(b) are sensitive to the size of the cell used, while the power laws seen at the larger times do not depend on the cell size.

In the nematiclike phase, i.e., for κ beyond κ_c, the correlations decay algebraically $g_\ell(r,0)\sim r^{-\eta_\ell}$ and $g_\ell(0,t)\sim t^{-\beta_\ell}$. There are pronounced finite size effects which lead to a flattening of the curves for $r\approx L/2$, limiting the range

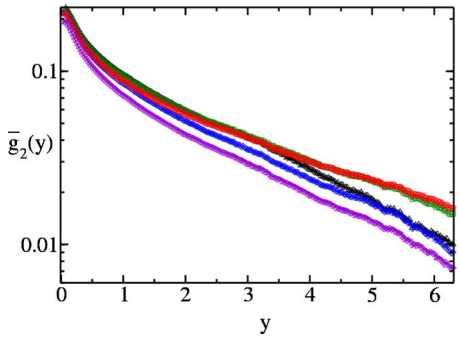

FIG. 11. (Color online) Correlation function in a (25×15)-sized system with a uniform κ gradient. Shown is the log-normal plot $\bar{g}_2(y)=\langle\cos\{2[\theta(y)-\theta(0)]\}\rangle-q_0^2$ for pairs of points in the same vertical strip of unit width. Curves from bottom to top correspond to different vertical strips in the order of increasing κ. It is evident from the plots that $\bar{g}_2(y)$ exhibits exponential decay. The distance y is in units of rod length.

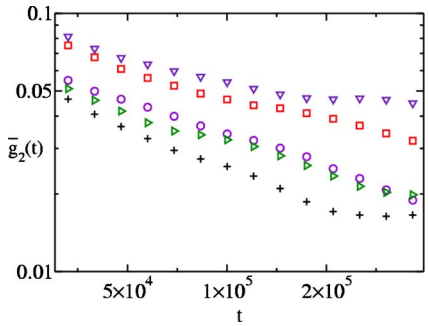

FIG. 12. (Color online) Dynamical correlation function in the system of Figs. 10 and 11. Log-normal plots of $\bar{g}_2(t)=\langle\cos\{2[\theta(t)-\theta(0)]\}\rangle-q_0^2$ as shown, with curves from bottom to top correspond to different cells with increasing κ (refer to the main text for details). The time t is in Monte Carlo time steps.

over which the power law behavior extends. We found that the values of the exponents η_ℓ and β_ℓ vary continuously with κ as shown in Table I. The estimations were done over ten independent sets of configurations, each averaged over 1000 configurations. For $\kappa\simeq\kappa_c$, we observed that $\eta_2\simeq0.23\pm0.03$ close to the predicted Kosterlitz-Thouless value 0.25. Our results for the static case agree with those reported by Frenkel and Eppenga [8] for the case of a fixed number of hard rods on a 2D plane. We confirm that at the critical point $\kappa=\kappa_c$ the mean density is $\simeq7$ [8].

For $\kappa>\kappa_c$, it was observed that exponents obtained from static correlations $g_2(r)$ and $g_4(r)$ are related through $\eta_2\simeq\eta_4/4$. It was also found that the exponents derived from the temporal correlations $g_2(t)$ and $g_4(t)$ are related in a similar way, i.e., $\beta_2\simeq\beta_4/4$. Further, the ratios $\eta_\ell/\beta_\ell\simeq2.0$ for $\ell=2$ and 4, implying that the dynamical exponent z_{dyn} is 2. These observations can be understood on the basis of the simple model discussed below.

In order to model the dynamics we note that the stochastic evaporation and deposition events change the local value of the coarse-grained angle field θ in a noisy, diffusive way. In the discussion below, we take the angle to be an unconstrained variable running from $-\infty$ to $+\infty$ with $(\theta+n\pi)$ denoting the same needle orientation for integer n. We consider a simple phenomenological equation

$$\frac{\partial\theta}{\partial t}=K\nabla^2\theta+\xi \tag{11}$$

where ξ denotes white noise which satisfies

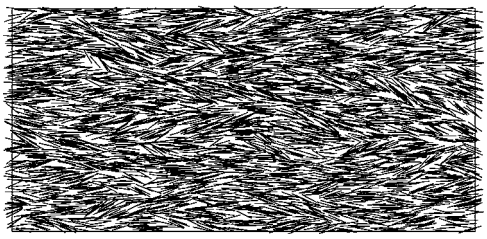

FIG. 13. A typical configuration for a (25×15)-sized system with a κ gradient achieved by varying the value of κ randomly around 32 in the X direction only. The horizontal alignment induced by the gradient is evident.

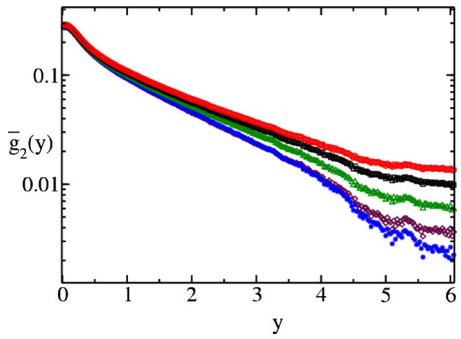

FIG. 14. (Color online) Correlation function in a (25×15)-sized system with a random κ gradient in the X direction only. Shown is the log-normal plot $\bar{g}_2(y)=\langle\cos\{2[\theta(y)-\theta(0)]\}\rangle-q_0^2$ for pairs of points in the same vertical strip of unit width. Curves from bottom to top correspond to different vertical strips in the order of increasing κ. It is evident from the plots that $\bar{g}_2(y)$ exhibits exponential decay. The distance y is in units of rod length.

$$\langle\xi(\mathbf{r},t)\xi(\mathbf{r}',t')\rangle = B\delta(\mathbf{r}-\mathbf{r}')\delta(t-t') \tag{12}$$

where B is a constant. This is of the same form as the Edwards-Wilkinson equation [25], which describes the evolution of a fluctuating interface. In our context, Eq. (11) follows from the symmetric form of the Frank free energy $F=\frac{1}{2}K\int(\nabla\theta)^2d\theta$ on using the phenomenological Langevin equation $\partial\theta/\partial t=-\delta F/\delta\theta+\xi$. A more complete description would involve coupled equations for the nonconserved density and orientational fields. From Eqs. (11) and (12) it follows that

$$\langle\theta(\mathbf{r}+\mathbf{r}',t+t')\theta(\mathbf{r},t)\rangle = \frac{B}{64\pi^5K}\int\frac{d^2k}{k^2}e^{i\mathbf{k}\cdot\mathbf{r}'}e^{-Kk^2t'}. \tag{13}$$

Setting $t'=0$ we find that

$$\langle[\theta(\mathbf{r}+\mathbf{r}',t)-\theta(r,t)]^2\rangle = \frac{B}{32\pi^5K}2\pi\ln(r) \tag{14}$$

which, using the Gaussian property of θ, further implies

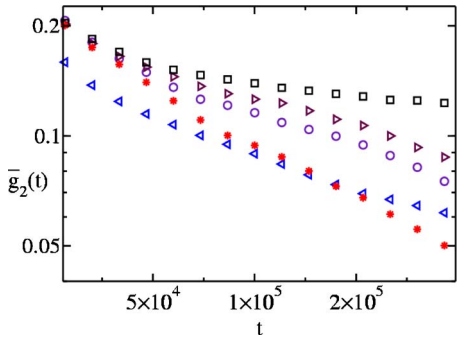

FIG. 15. (Color online) Dynamical correlation function in the system of Figs. 13 and 14. Log-normal plots of $\bar{g}_2(t)=\langle\cos\{2[\theta(t)-\theta(0)]\}\rangle-q_0^2$ as shown, with curves from bottom to top corresponding to different cells with increasing κ. The time t is in Monte Carlo time steps.

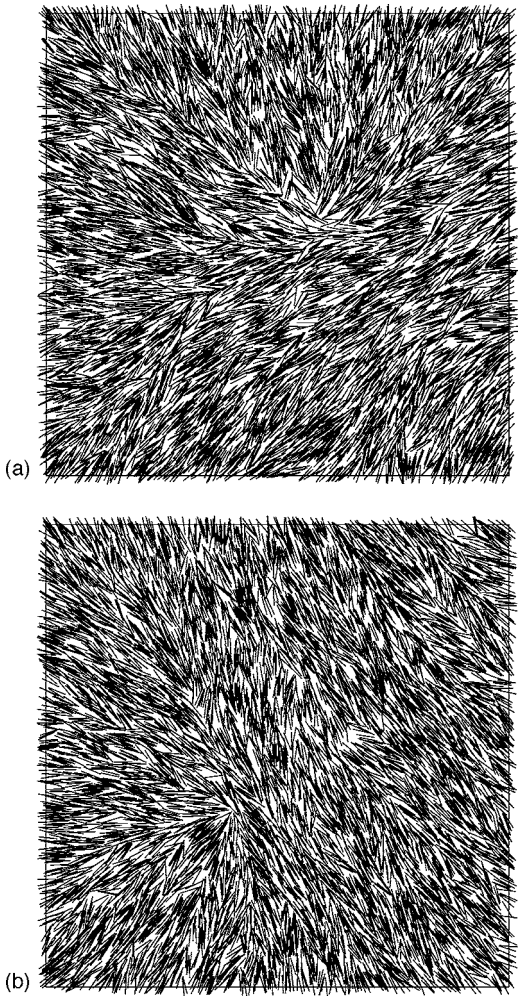

FIG. 16. Snapshots of hard-rod configurations for random binary distribution of κ values 27 and 50 on the substrate of size 25×25. Representative configurations characterizing two different states [(a) and (b)] which are reached from different initial conditions, for the same κ distribution.

$$\langle\cos\{\ell[\theta(\mathbf{r}+\mathbf{r}',t)-\theta(r,t)]\}\rangle \simeq r^{-\eta_\ell} \tag{15}$$

where $\eta_\ell=\ell^2B/32\pi^4K$. The measured values of η_ℓ can be used to find K/B, whose value is included in Table I.

Similarly, setting $r'=0$ in Eq. (13) we find the autocorrelation function

$$\langle\cos\{\ell[\theta(\mathbf{r},t+t')-\theta(r,t)]\}\rangle \simeq t^{-\beta_\ell} \tag{16}$$

where $\beta_\ell=\ell^2B/64\pi^4K$. Thus, for all $\kappa>\kappa_c$ the ratio of η_4 to η_2 (and β_4 to β_2) is expected to be 4; as we have seen above, our numerical results confirm this. Also, we find the dynamical exponent $z_{\rm dyn}=\eta_\ell/\beta_\ell$ is $\simeq2.0$.

IV. EFFECT OF INHOMOGENEOUS κ

In this section, we explore the effects of having a spatial variation of the deposition-evaporation rate ratio κ. In a physical system, such a variation could arise from the variation of the chemical potential or substrate temperature from one spot to another as their local values could influence the

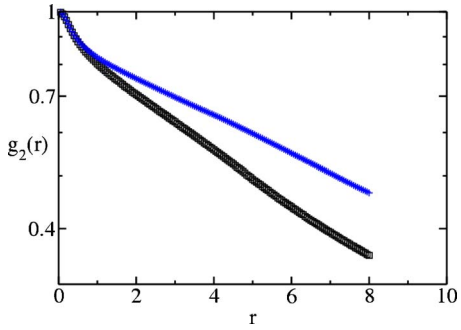

FIG. 17. (Color online) Evidence for exponential decay of spatial correlations in a system with random binary distribution of κ. The figure shows log-normal plots of $g_2(\mathbf{r})=\langle\cos\{2[\theta(\mathbf{r})-\theta(0)]\}\rangle$. The parameters are the same as in Fig. 16, and the curves correspond to the different steady states evolved from two different initial conditions. The distance r is in units of rod length.

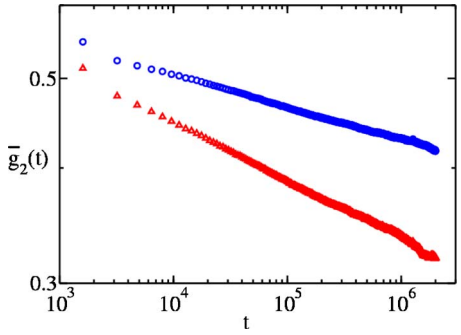

FIG. 18. (Color online) Evidence for a power-law decay of temporal correlations in a system with random binary distribution of κ. The figure shows log-log plots of $\bar{g}_2(t)=\langle\cos\{2[\theta(t)-\theta(0)]\}\rangle-q_0^2$. The parameters are the same as in Fig. 16, and the curves are obtained in the different steady states reached from two different initial conditions. The time t is in Monte Carlo time steps.

local detachment rate, as seen from Eq. (7). As expected, such changes in κ induce a spatial variation of the density; more interestingly, they have a strong effect on the orientational order as well. We explore these effects by considering several types of spatial variations of κ.

In parallel to the discussion in Sec. II, let $\Gamma_d(x)$ and $\Gamma_e(x)$ denote the deposition and evaporation rates at point x in the plane, and let $\kappa(x)=\Gamma_d(x)/\Gamma_e(x)$. Let C' be the configuration reached from configuration C by removing the rod at x_m and let $P(C')$ and $P(C)$ be the weights of the respective configurations in steady state. We can check that the condition of detailed balance is valid when $P(C)$ has the product form $P(C)=\Pi_i z(x_i)$ where $z(x_i)=\Lambda^2\rho(x_i)\kappa(x_i)$ is the local fugacity at the location of the ith rod. If C' is obtained from C by evaporating the mth rod, then evidently $P(C)=P(C')z(x_m)$. Recalling that $W(C'\to C)=\Gamma_d(x_m)$ and $W(C\to C')=\Gamma_e(x_m)$, we see that the condition of detailed balance is valid.

Thus the system reaches an equilibrium steady state which, however, is inhomogeneous in density, due to the nonuniform position dependence of κ. The nature of orientational order depends strongly on the the way in which κ is specified to vary over the plane. Below we consider several types of variations.

(i) A single interface separating low and high κ regions,

$$\kappa(x)=\kappa_1 \quad \text{for } x<\frac{L}{2},$$

$$\kappa(x)=\kappa_2 \quad \text{for } x>\frac{L}{2}.$$

(ii) A uniform gradient in κ across the substrate,

$$\kappa(x)=\kappa_1\left(1+\alpha\frac{x}{L}\right).$$

(iii) Random variation of κ in the X direction only,

$$\kappa(x)=\kappa_1+\delta\kappa(x),$$

where $\delta\kappa(x)<\kappa_1$ is a random function of x.

(iv) A random binary assignment of κ on a grid on the 2D substrate.

In the first three cases, periodic boundary conditions were applied in the Y direction and open boundary conditions along X. In the last case, open boundaries were used in both directions. In all the cases considered, the ranges of κ values were chosen to be above κ_c, the critical value in the uniform case. Our findings are as follows.

A. κ_1-κ_2 interface

Here, a uniform value κ_1 operates up to halfway across the 2D plane along the X direction, while $\kappa=\kappa_2$ $(>\kappa_1)$ in the remaining half. In the vicinity of the interfacial region, the rods are observed to orient in the direction the of κ gradient, i.e., perpendicular to the interface [see Fig. 6(a)].

This can be understood on entropic grounds. That arrangement of rods is favored which maximizes the entropy. By symmetry, the preferred average orientation of rods should be either (a) parallel or (b) perpendicular to the interface. Consider those rods in the high κ half, whose centers lie very close to the interface (within half a rod length) so that part of such rods can reach into the low density side. Small variations in the angle of each rod would contribute to the entropy, but these are limited by the presence of other rods. A horizontal average alignment allows the rods to sample a less dense environment, and thus be subject to fewer constraints, on one side. Thus, option (b) would be preferred over (a). The effect of interface-induced horizontal alignment is felt for some distance away from the interface on both sides. This is evident in Fig. 6(a), which shows a steady state configuration in a system of size 25×25 (in units of rod length), with $\kappa_1=30$ and $\kappa_2=50$. However, for a large enough size, the system reverts to a power-law phase in the region far from the interface as observed in the uniform κ case. The correlation function decays as a power law in the bulk, away from the interface, as shown in Fig. 6(b).

We also considered the case with two values of κ, using periodic boundary conditions in both directions which leads to two interfaces (Fig. 7). The figure shows an (80×15)-sized system with periodically linked left and right quarters with $\kappa_1=30$, while the middle half has $\kappa_2=50$. Evidently, this system too shows interface-induced horizontal

alignment. This geometry admits of an interesting limit where the entropy-driven alignment is particularly clear. On shrinking the width of the central region to zero, at the same time taking the limit $\kappa_1 \to 0$, we obtain a 1D model as a limiting case. In this model, deposition and evaporation moves are allowed with needle centers constrained to lie on the line. Needles are found to orient preferentially perpendicular to the line (see the inset in Fig. 8). The reason is evident. If the mean orientation of the director is perpendicular to the substrate, needles have the largest leeway to make angular excursions about the mean, i.e., the rotational entropy is then the largest. The variation with κ of the density and order parameter $q=\langle \cos 2\phi \rangle$ where ϕ is the angle made with the direction perpendicular to the line, is shown in Fig. 8.

A similar effect should also lead to rods getting aligned horizontally if they are close to an open boundary in the 2D system. That this is so can be seen in Fig. 9, which shows a system with uniform $\kappa=27$ and open boundary conditions along the X direction.

B. Uniform κ gradient

This case is related to the discussion above, as the linear increase in κ may be viewed as a continuous succession of interfaces from one end to the other. Since each interface induces an alignment of rods across it, this results in overall alignment of the rods in the system (see Fig. 10). Note that the alignment is not an outcome of spontaneous breaking of orientational symmetry, as the gradient in κ singles out a direction in space. We checked that the horizontal alignment is not tied to the aspect ratio of the container by simulating a system size 10×40, and observing overall horizontal alignment of rods in the steady state.

Figure 10 shows a steady state configuration in a system of size 25×15, with κ varying linearly from a value $\kappa_L=32$ at the left end to a value $\kappa_R=50$ at the right end. In our simulations, the system was equilibrated for 10^7 Monte Carlo steps and 10^4 postequilibration configurations were used to calculate averages. We studied the spatial and dynamical behavior of the orientational correlation function $g_2(r,t)=\langle \cos\{2[\theta(r,t)-\theta(0,0)]\}\rangle$. Since the system is inhomogeneous along the X direction, the substrate was divided into vertical strips, each having width of a rod length, and each strip was studied separately. The Y density of needles inside each strip was uniform though the density varies from strip to strip. We monitored the correlation function $g_2(y)=\langle \cos\{2[\theta(y+y_0)-\theta(y_0)]\}\rangle$ (see Fig. 11), and found that $g_2(y)$ decays exponentially to a nonvanishing constant value q_0 which differs from strip to strip. For the system under study, q_0^2 varies in the range 0.68–0.77 over the strips.

The dynamical correlation function, i.e., $g_2(t)=\langle \cos\{2[\theta(t)-\theta(0)]\}\rangle$ was calculated by coarse graining. The system was divided into number of small cells (2×2) and an average value of orientation was assigned to each cell by averaging over needles in it. The plot of $g_2(t)$ is shown in Fig. 12 for cells at different values of X. Each curve shows an exponential approach to a nonzero constant value. The behavior of both the spatial and dynamical orientational parts of the correlation functions indicates a phase with overall orientational alignment.

C. Random variation of $\kappa(x)$

We have seen that a uniform gradient in κ results in an orientationally ordered state. However, the argument for ordering does not depend on the gradient being constant in magnitude or sign. Thus, if κ varies randomly (with $\kappa > \kappa_c$) along the X direction but is uniform along Y, the resulting state once again should exhibit horizontal alignment with needles aligned along the X direction. The resulting state can once again be viewed as a continuous succession of interfaces and should display overall alignment.

Figure 13 shows a steady state configuration obtained with a quenched random variation of $\kappa(x)$. The system was simulated by varying κ randomly around a value of κ such that $\kappa \pm \delta\kappa(x) > \kappa_c$, where $\delta\kappa(x)$ denotes random variations along the X direction. We used $\kappa \simeq 32$ and $\delta\kappa=2.0$. The correlation functions $g_2(y)$ and $g_2(t)$ behave similarly to the uniform gradient case (see Figs. 14 and 15). Thus, this case also yields a phase with overall orientational alignment.

D. 2D random binary distribution of κ values

In this case, the fugacity is set inhomogeneously in a quenched disordered fashion, so that the tendency to align locally along gradients results in competing patterns of order, i.e the system is frustrated. The resulting state has glassy features and contains domains of different orientations (see Fig. 16) [26].

In our simulations, we divided the substrate of size 25×25 into a grid of unit length squares. Each square was randomly assigned a κ value either 27 or 50 (both greater than κ_c). The random κ gradient across square edges generates local disorder, which can disrupt the orientational order and result in destruction of orientational alignment on the scale of the system size. The effect of quenched random disorder due to orientational randomness of cross links in a system of nematic elastomers has been studied earlier [27] and the model was reported to have spin-glass-like behavior. In our model, the disorder emerges from the randomness in the spatial distribution of κ values. We find that the spatial correlation $g_2(r)$ decays exponentially to zero (Fig. 17) whereas the dynamical part $g_2(t)$ seems to decay in an algebraic manner to a nonzero value (Fig. 18).

The behavior is suggestive of a glassy system which is disordered in space but relaxes slowly in time. Moreover, it was also found that with same quenched disorder arrangement, different initial conditions lead to different states. Typical configurations in each of these states are shown in Fig. 16, which is a glasslike feature.

V. CONTINUUM DESCRIPTION

As discussed above, our simulations show that a spatially inhomogeneous deposition-evaporation ratio κ can induce nematic order and other interesting orientational patterns in the equilibrium state of a system of hard needles. It is interesting to ask whether these effects can be captured within a

phenomenological coarse-grained description based on including symmetry-allowed terms in the free energy. In the context of liquid crystals, such an approach has proved successful in studying large distance phenomena, including the effects of walls and other inhomogeneities [2]. Below we sketch such a description for our system of interest [28]. Besides showing that gradients in the deposition-evaporation rates lead to orientational ordering, the treatment suggests the occurrence of local splay.

Let us define a nematic director field $\hat{n}(r)$ to describe the local coarse-grained value of the orientation of needles [evidently, $\hat{n}(r)$ and $-\hat{n}(r)$ describe the same configuration]. In the absence of externally imposed inhomogeneities, spatial variations of $\hat{n}(r)$ lead to a free energy described by the Frank form [2]

$$F_K = \int d^2r \left(\frac{K_1}{2} (\nabla \cdot \hat{n})^2 + \frac{K_3}{2} [\hat{n} \times (\nabla \times \hat{n})]^2 \right). \quad (17)$$

The two terms describe, respectively, contributions of splay and bend to the free energy; there is no contribution from twist in 2D.

Inhomogeneities in deposition-evaporation rates lead to spatial gradients $\nabla\kappa$, which imply additional terms in the free energy. These terms consist of scalars involving $\nabla\kappa$ and $\hat{n}$, respecting invariance under $\hat{n} \leftrightarrow -\hat{n}$. Two such scalars are obtained by replacing the gradient operator by $\nabla\kappa$ in the terms in Eq. (17) to get

$$F_J = \int d^2r \frac{J_1}{2} [(\nabla\kappa \cdot \hat{n})^2] + \int d^2r \frac{J_3}{2} \{[\hat{n} \times (\nabla\kappa \times \hat{n})]^2\}. \quad (18)$$

In addition to these terms, which are quadratic in $\nabla\kappa$, one can also construct scalars which involve $\nabla\kappa$ linearly [29]

$$F_L = \int d^2r \frac{L_1}{2} \nabla\kappa \cdot [\hat{n}(\nabla \cdot \hat{n})] + \int d^2r \frac{L_3}{2} \nabla\kappa \cdot [(\hat{n} \cdot \nabla)\hat{n}]. \quad (19)$$

Symmetry considerations alone do not suffice to determine the values of the coefficients K_1, K_3, J_1, J_3, L_1, and L_3. Their density dependences can be found on noting that a change in κ induces a change in density, thereby influencing the elastic energy. To incorporate this, we replace $\hat{n}$ in Eq. (17) by $[\rho(r)\hat{n}/\rho_0]$ where $\rho(r)$ and ρ_0 are the local and average densities, respectively. The Appendix contains the resulting form of the free energy F_ρ and the values of the coupling constants.

Let us turn to the consequences of the new terms. With a uniform spatial gradient, $\nabla\kappa = \alpha\hat{x}$ [case (ii) above], F_J induces overall alignment of needles. To see this, consider $F_K + F_J$. Evidently, F_K is minimized by any arrangement in which $\hat{n}$ is uniform in space while F_J is orientation dependent. Writing $\hat{n} = \hat{x}\cos\phi + \hat{y}\sin\phi$, we find

$$F_J = \alpha^2 (J_1 \cos^2\phi + J_3 \sin^2\phi). \quad (20)$$

$F_K + F_J$ is minimized by having an aligned state, either with $\phi = 0$ (if $J_3 > J_1$) or with $\phi = \pi/2$ (if $J_3 < J_1$). Our numerical results, supported by the entropic considerations given above, show alignment in the direction of the gradient, implying $\Delta J \equiv J_3 - J_1$ is positive.

Now consider the effect of F_L. Setting $\nabla\kappa = \alpha\hat{x}$ in Eq. (19), we find

$$F_L = -\alpha(L_1 + L_3)\sin\phi\cos\phi \frac{\partial\phi}{\partial x} + \alpha(L_1\cos^2\phi - L_3\sin^2\phi)\frac{\partial\phi}{\partial y}. \quad (21)$$

$(F_K + F_L)$ can be minimized on noting that each of the L_1 and L_3 terms is an eigenfunction of the Frank elastic matrix. The result is

$$\frac{\partial\phi}{\partial y} = \frac{-L_1}{K_1}\cos^2\phi + \frac{L_3}{K_3}\sin^2\phi, \quad (22)$$

$$\frac{\partial\phi}{\partial x} = \left(\frac{L_1}{K_1} + \frac{L_3}{K_3}\right)\cos\phi\sin\phi. \quad (23)$$

These terms describe a spiraling tendency of the director in space.

The full problem involves minimizing $F_J + F_K + F_L$. If F_J is dominant, the director is primarily aligned along the gradient implying ϕ is small. Equations (22) and (23) then reduce to $\partial\phi/\partial y \approx -L_1/K_1$ which describes a spiraling director; further, F_J restricts angular excursions to be at most $\phi_0 \propto 1/\sqrt{\Delta J}$. Thus the predicted state is one with overall alignment along the gradient, but with local splay structures, each with a small opening angle $\simeq 2\phi_0$. This picture is borne out by our simulations.

For case (iii) in which $\kappa(x)$ varies randomly, we see that $F_J = \overline{\alpha^2}(J_1\cos^2\phi + J_3\sin^2\phi))$ where $\overline{\alpha^2}$ is the spatial average of the mean squared gradient. As for case (ii), the free energy is minimized by having a state with alignment along the gradient, as observed in our simulations, provided $J_3 > J_1$.

In case (iv), the gradients that appear in Eq. (18) are random in direction leading to frustration in the arrangement of needles. Equations (17)–(19) provide a starting point for a theoretical description of the glassy state.

VI. CONCLUSION

In summary, we have studied orientational ordering in a 2D grand canonical system of hard rods using deposition and evaporation moves. The control parameter is the ratio κ of deposition and evaporation rates, which controls the density. The system with uniform κ displays a transition from an isotropic phase (for $\kappa < \kappa_c$) to a phase characterized by algebraically decaying static and dynamical orientational correlations for $\kappa > \kappa_c$. Further, the values of the critical exponents and the behavior of the orientational cumulant are consistent with Kosterlitz-Thouless theory. The numerical results for the dynamical correlation functions are described by a phenomenological Edwards-Wilkinson equation for the nonconserved orientational field.

Our principal results pertain to the behavior induced by having a position-dependent κ, and hence a space-varying density of rods. An anisotropic variation of κ (say along the

X direction only) results in needles aligning along the κ gradient. This was understood by first considering the effect of an interface separating regions with two values of κ. Entropic considerations lead the needles to align normal to the interface, i.e., along the gradient. From another point of view, κ gradients lead to additional terms in the Frank-like free energy and these in turn imply orientational ordering. Finally, in a system with quenched disorder corresponding to spatially random κ, we found indications of orientationally frozen states with glasslike characteristics. It would be useful to have a better characterization and understanding of this glassy state.

The mechanism behind gradient-induced orientational ordering is simple: spatial variations of κ induce variations in needle density; and an average alignment of needles along the gradient is preferred as this leads to an enhanced entropy of rotational excursions around the mean. In effect, the κ gradient thus behaves like an external field acting to produce nematic order, ultimately due to the strong coupling between spatial and orientational degrees of freedom in the needle system. Gradient-induced ordering effects should be present in three-dimensional systems as well. In 3D, the Onsager mechanism for nematic long range order would predict ordering for values of a uniform κ exceeding a critical value κ_c. The addition of a uniform κ gradient would be expected to lead to a nonzero value of nematic ordering for all values of κ, and to enhance its value for $\kappa > \kappa_c$. It would be interesting to test this prediction, and have a quantitative measure of gradient-induced ordering in 3D.

ACKNOWLEDGMENTS

We acknowledge very useful discussions with Yashodhan Hatwalne, Sriram Ramaswamy, and Gautam Menon. We thank Deepak Dhar for a critical reading of the manuscript and suggestions.

APPENDIX

To incorporate the effect of spatial variation of the density, we write $[\rho(r)\hat{n}/\rho_0]$ in place of the director $\hat{n}$ in the Frank free energy F_K of Eq. (17). The resulting expression F_ρ for the free energy can be written as

$$F_\rho = \int d^2r \left(\frac{K_1}{2\rho_0^2} (\boldsymbol{\nabla} \cdot \rho\hat{n})^2 + \frac{K_3}{2\rho_0^4} [\rho\hat{n} \times (\boldsymbol{\nabla} \times \rho\hat{n})]^2 \right). \tag{A1}$$

The expansion of the integrand involves ten terms:

$$\begin{aligned}
&\left[\frac{K_1}{2\rho_0^2}\rho^2 \sin^2\phi + \left(\frac{K_3}{2\rho_0^4}\rho^2 \right) \rho^2 \cos^2\phi \right] (\partial\phi/\partial x)^2 + \left[\frac{K_1}{2\rho_0^2}\rho^2 \cos^2\phi + \left(\frac{K_3}{2\rho_0^4}\rho^2 \right) \rho^2 \sin^2\phi \right] (\partial\phi/\partial y)^2 \\
&+ \left[\frac{K_1}{2\rho_0^2} \cos^2\phi + \left(\frac{K_3}{2\rho_0^4}\rho^2 \right) \sin^2\phi \right] (\partial\rho/\partial x)^2 + \left[\frac{K_1}{2\rho_0^2} \sin^2\phi + \left(\frac{K_3}{2\rho_0^4}\rho^2 \right) \cos^2\phi \right] (\partial\rho/\partial y)^2 \\
&+ \left[\frac{-K_1}{2\rho_0^2} + \left(\frac{K_3}{2\rho_0^4}\rho^2 \right) \right] 2\rho \sin\phi \cos\phi (\partial\phi/\partial x)(\partial\rho/\partial x) + \left[\frac{K_1}{2\rho_0^2} \left(\frac{K_3}{2\rho_0^4}\rho^2 \right) \right] 2\rho \sin\phi \cos\phi (\partial\phi/\partial y)(\partial\rho/\partial y) \\
&+ \left[\frac{K_1}{2\rho_0^2} - \left(\frac{K_3}{2\rho_0^4}\rho^2 \right) \right] 2 \sin\phi \cos\phi (\partial\rho/\partial x)(\partial\rho/\partial y) + \left[\frac{-K}{2\rho_0^2} + \left(\frac{K_3}{2\rho_0^4}\rho^2 \right) \right] 2\rho^2 \sin\phi \cos\phi (\partial\phi/\partial x)(\partial\phi/\partial y) \\
&+ \left[\frac{-K_1}{2\rho_0^2} \sin^2\phi - \left(\frac{K_3}{2\rho_0^4}\rho^2 \right) \cos^2\phi \right] 2\rho(\partial\phi/\partial x)(\partial\rho/\partial y) + \left[\frac{K_1}{2\rho_0^2} \cos^2\phi + \left(\frac{K_3}{2\rho_0^4}\rho^2 \right) \sin^2\phi \right] 2\rho(\partial\rho/\partial x)(\partial\phi/\partial y).
\end{aligned}$$

In case (ii) where κ varies linearly with x, the density gradient is nonzero only along the *X* direction, and vanishes along *Y*, so the terms involving $\partial\rho/\partial y$ do not contribute. We can then read off the density dependence induced in the elastic constants in terms of the original Frank's constants as

$$K_1'(\rho) - \frac{K_1}{\rho_0^2}\rho^2 \quad \text{and} \quad K_3'(\rho) = \frac{K_3}{\rho_0^4}\rho^4.$$

Now, comparing the third term of the expression with Eq. (18) and writing $\partial\rho/\partial x = \alpha\zeta(\rho)$ where $\zeta(\rho) = \partial\rho/\partial\kappa$, we have

$$J_1(\rho) = \frac{K_1}{\rho_0^2}[\zeta(\rho)]^2, \quad J_3(\rho) = \frac{K_3}{\rho_0^4}\rho^2[\zeta(\rho)]^2. \tag{A2}$$

Similarly, grouping the fifth and the tenth terms together and comparing with Eq. (19), we obtain

$$L_1(\rho) = \frac{K_1}{\rho_0^2} 2\rho\zeta(\rho), \quad L_3(\rho) = \left(-\frac{K_3}{\rho_0^4}\rho^2 \right) 2\rho\zeta(\rho). \tag{A3}$$

[1] S. Fraden *et al.*, Phys. Rev. Lett. **63**, 2068 (1989).
[2] P. G. de Gennes and J. Prost, *The Physics of Liquid Crystals*, 2nd ed. (Clarendon, Oxford, 1993).
[3] M. F. Islam *et al.*, Phys. Rev. Lett. **92**, 088303 (2004).
[4] J. A. Cuesta and D. Frenkel, Phys. Rev. A **42**, 2126 (1990).
[5] A. Stroobants, H. N. W. Lekkerkerker, and D. Frenkel, Phys. Rev. A **36**, 2929 (1987).
[6] M. A. Bates and D. Frenkel, J. Chem. Phys. **112**, 10034 (2000).
[7] M. C. Lagomarsino, M. Dogterom, and M. Dijkstra, J. Chem. Phys. **119**, 3535 (2003).
[8] D. Frenkel and R. Eppenga, Phys. Rev. A **31**, 1776 (1985).
[9] J. W. Evans, Rev. Mod. Phys. **65**, 1281 (1993).
[10] E. Frey and A. Vilfan, Chem. Phys. **284**, 287 (2002).
[11] V. Narayan, N. Menon, and S. Ramaswamy cond-mat/0510082 (unpublished).
[12] R. B. Stinchcombe, M. D. Grynberg, and M. Barma, Phys. Rev. E **47**, 4018 (1993).
[13] P. L. Krapivsky and E. Ben-Naim, J. Chem. Phys. **100**, 6778 (1994).
[14] A. J. Kolan, E. R. Nowak, and A. V. Tkachenko, Phys. Rev. E **59**, 3094 (1999).
[15] P. R. Van Tassel *et al.*, J. Chem. Phys. **112**, 1483 (2000).
[16] J. Talbot, G. Tarjus, and P. Viot, Phys. Rev. E **61**, 5429 (2000).
[17] Lj. Budinski-Petkovic and U. Kozmidis-Lubiric, Physica A **301**, 174 (2001).
[18] L. Onsager, Ann. N.Y. Acad. Sci. **51**, 627 (1949).
[19] J. P. Straley, Phys. Rev. A **4**, 675 (1971).
[20] D. R. Nelson, in *Phase Transitions and Critical Phenomena*, edited by C. Domb and J. L. Lebowitz (Academic London, 1983), Vol. 7.
[21] D. P. Landau and K. Binder, *A Guide to Monte Carlo Simulations in Statistical Physics* (Cambridge University Press, Cambridge, U.K., 2000), Sec. 6.1.3.
[22] K. Binder, in *Monte Carlo Methods in Statistical Physics: An Introduction*, edited by K. Binder and D. W. Heermann (Springer, Berlin, 1988).
[23] For instance, for Ising-like systems, for $T > T_c$ and $L \gg \xi$, $P_L(s)$ approaches a Gaussian distribution, while for $T < T_c$ and $L \gg \xi$, $P_L(s)$ approaches two Gaussians centered at $\pm M_0$ where ξ denotes the correlation length and M_0 is the spontaneous magnetization of infinite system. At criticality, $P_L(s)$ approaches a scaled universal form for large L [22]. Note that s denotes the order parameter corresponding to Ising-like systems.
[24] H. Weber, D. Marx, and K. Binder, Phys. Rev. B **51**, 14636 (1995).
[25] S. F. Edwards and D. R. Wilkinson, Proc. R. Soc. London, Ser. A **381**, 17 (1982).
[26] K. Binder, in *Spin Glasses and Random Fields*, edited by A. P. Young (World Scientific, Singapore, 1997).
[27] Y.-K. Yu, P. L. Taylor, and E. M. Terentjev, Phys. Rev. Lett. **81**, 128 (1998).
[28] We are grateful to Yashodhan Hatwalne, Gautam Menon, and Sriram Ramaswamy for very useful inputs on this section.
[29] The form of these terms is the same as those describing the coupling of a flexoelectric nematic to the electric field; see Sec. 3.3.2 of Ref. [2]. In our case, the external field is $\nabla\kappa$.